JOURNAL OF THERMOPHYSICS AND HEAT TRANSFER
Vol. 24, No. 3, July–September 2010

Direct Numerical Simulation of the Turbulent Ekman Layer: Turbulent Energy Budgets

Stuart W. Marlatt,* Scott B. Waggy, and Sedat Biringen†
University of Colorado, Boulder, Colorado 80309

DOI: 10.2514/1.45200

Results from a direct numerical simulation of the Ekman layer at a Reynolds number of 400 were analyzed to compute energy spectra and energy budgets for this flow. Turbulent kinetic energy spectra show evidence of isotropy at high wave numbers. Energy budgets indicated that the majority of the turbulent kinetic energy in the flow is produced by the coupling between the streamwise primary Reynolds shear stress and the streamwise velocity gradient. It was also found that the coupling of the vertical velocity variance with the spanwise directions allows transfer of kinetic energy by means of the return-to-isotropy pressure strain terms due to the splatting effect.

Nomenclature

A_{ik}	=	advection by mean shear
b	=	buoyancy parameter
C_{ik}	=	Coriolis redistribution
D_{ik}	=	molecular diffusion
F_e	=	Fourier spectra for total kinetic energy
F_{uu}, F_{vv}, F_{ww}	=	Fourier spectra for streamwise, spanwise, and vertical velocity components
f	=	Coriolis parameter
g	=	acceleration of gravity
L_x, L_y, L_z	=	length of domain in streamwise, spanwise, and vertical directions
M_{ik}	=	molecular diffusion and dissipation
N_x, N_y, N_z	=	number of grid points in streamwise, spanwise, and vertical directions
P_{ik}	=	production/destruction by mean shear stresses
p	=	pressure
Re	=	Reynolds number
Ro	=	Rossby number
Pr	=	Prandtl number
T_{ik}	=	turbulent diffusion
U_g	=	geostrophic freestream velocity
u, v, w	=	velocity components in streamwise, spanwise, and vertical directions
u_*	=	surface friction velocity
u', v', w'	=	perturbation velocity components in streamwise, spanwise, and vertical directions
x, y, z	=	spatial coordinate in streamwise, spanwise, and vertical directions
z^+	=	vertical coordinate in terms of wall units
α_{total}	=	total horizontal wave number
α_x, α_y	=	wave numbers in streamwise and spanwise directions
β	=	surface shear stress direction
β_{ik}	=	buoyant production/destruction
γ_{uu}, γ_{vv}, γ_{ww}, γ_e	=	orientation angles of u, v, w, and kinetic energy spectra
Δt	=	computational time step
Δx^+, Δy^+, Δz^+	=	mesh spacing in streamwise, spanwise, and vertical directions in terms of wall units
δ	=	neutral-layer turbulent depth
δ_E	=	Ekman-layer thickness
ε_{ik}	=	viscous dissipation
Θ_{ik}	=	pressure diffusion
θ	=	nondimensional temperature
κ	=	coefficient of thermal diffusivity
ν	=	kinematic viscosity
Π_{ik}	=	pressure-gradient/velocity correlation
ρ	=	fluid density
τ_w	=	shear stress at the wall
Φ_{ik}	=	pressure strain
Ω	=	vertical component of rotation

Received 5 June 2009; revision received 20 March 2010; accepted for publication 28 March 2010.

*Currently United Launch Alliance, Littleton, CO 80120.
†Department of Aerospace Engineering Sciences (Corresponding Author).

I. Introduction

RESULTS from a direct numerical simulation (DNS) of the neutrally stratified turbulent Ekman layer are presented. A major goal of this study is to analyze the turbulent energy budgets. Since no turbulence closure model is required for a DNS, the turbulent energy budgets are determined directly from calculated instantaneous, three-dimensional velocity-pressure field. The conditions of this simulation are relevant to the atmospheric boundary layer (ABL), although purely neutral stratification conditions are not frequently observed in the natural atmosphere. While the mean potential temperature profile may be locally neutral, convective motion from overlying or underlying regions will generally initiate motion that advects fluid from these areas through the neutrally stratified region [1]. Consequently, a fundamental motivation for the present simulation is to provide a solid baseline against which effects of capping stable stratification may be assessed. To this end, the results of the neutral Ekman-layer simulation will be analyzed in considerable detail.

The present study extends the findings of Coleman et al. [2], considering other aspects of this flow. In particular, the present evaluation of the neutral Ekman layer examines the energy balances of all the Reynolds stress terms and uncovers new aspects of intercomponent energy transfer mechanisms in this complex turbulent flow.

II. Flowfield and Numerical Solution Methodology

A. Physical Description of Flow

The governing equations in conservative form for the time-varying incompressible flowfield are given below in Eq. (1):

$$\frac{\partial u}{\partial x}+\frac{\partial v}{\partial y}+\frac{\partial w}{\partial z}=0$$

$$\frac{\partial u}{\partial t}+\frac{\partial uu}{\partial x}+\frac{\partial uv}{\partial y}+\frac{\partial uw}{\partial z}-\frac{1}{Ro}v=-\frac{\partial p}{\partial x}+\frac{1}{Re}\nabla^2 u$$

$$\frac{\partial v}{\partial t}+\frac{\partial uv}{\partial x}+\frac{\partial vv}{\partial y}+\frac{\partial vw}{\partial z}+\frac{1}{Ro}u=-\frac{\partial p}{\partial y}+\frac{1}{Re}\nabla^2 v$$

$$\frac{\partial w}{\partial t}+\frac{\partial uw}{\partial x}+\frac{\partial vw}{\partial y}+\frac{\partial ww}{\partial z}=-\frac{\partial p}{\partial z}+\frac{1}{Re}\nabla^2 w+b$$

$$\frac{\partial b}{\partial t}+\frac{\partial ub}{\partial x}+\frac{\partial vb}{\partial y}+\frac{\partial wb}{\partial z}=\frac{1}{RePr}\nabla^2 b \qquad (1)$$

In the above expressions u, v, and w are the velocities in the x, y, and z Cartesian directions; p is the pressure; b is the buoyancy given by $b = g\delta_E\theta/U_g^2$ (where g is the gravitational constant, δ_E is the Ekman-layer depth, θ is the dimensionless temperature, and U_g is the geostrophic freestream velocity); Re is the Reynolds number defined by $Re = U_g\delta_E/\nu$; Pr is the Prandtl number given by $Pr = \nu/\kappa$ (where κ is the coefficient of thermal diffusivity); and Ro is the Rossby number, given by $U_g/(f\delta_E)$ (where $f = 2\Omega$ and Ω is the vertical component of rotation.

The direct numerical simulation results described here addressed a neutrally stratified turbulent Ekman layer of Reynolds number $Re = 400$ [3]. These conditions match those modeled by a number of other researchers (e.g., Coleman et al. [2]). At this relatively low Reynolds number, the flow is turbulent but the turbulent energy spectrum does not fully present the inertial subrange characteristic of fully developed turbulent flows (e.g., see [4]). Nevertheless, many of the turbulence statistics computed from the present simulations are qualitatively (and quantitatively in most cases) similar to ABL observations. Since the direct simulation results are free from the uncertainties introduced by subgrid-scale turbulence parameterization schemes, DNS studies provide a valuable insight into the details of the turbulent flow dynamics. This is particularly true in the near-wall region, where the accuracy of most turbulence models is relatively poor.

B. Direct Numerical Simulation Specifications

The DNS solver used in the present work incorporates a third-order split-step Runge–Kutta time integration scheme. Periodic boundary conditions in the spanwise and streamwise directions allow the corresponding derivatives to be calculated pseudospectrally in the horizontal plane. A stretched and staggered vertical mesh is incorporated to cluster grid points near the wall. Vertical diffusion derivatives used fourth-order finite differences. Vertical-direction advective derivatives used fifth-order upwind-biased differences. The lower surface incorporates a no-slip boundary condition, and the top boundary is stress-free, so that

$$\frac{\partial u}{\partial z}=\frac{\partial v}{\partial z}=0; \qquad w=0$$

Specifications for the two cases analyzed are included in Table 1. Note that case B uses twice the mesh resolution as case A in both the streamwise x and spanwise y directions. This grid spacing (in terms of wall units) is comparable to other Ekman-layer DNS studies [5,6]. The vertical mesh distribution was clustered around the wall region with about 12 grid points in the viscous sublayer ($z^+ \leq 5$).

Table 1 Case parameters

Case	Re	$L_x = L_y$	L_z	$N_x = N_y$	N_z	$\Delta x^+ = \Delta y^+$	$\Delta z^+_{\min}$	Δt
A	400	$26\delta_E$	$34\delta_E$	64	80	10.7	$\sim$0.6	0.1
B	400	$26\delta_E$	$34\delta_E$	128	80	5.3	$\sim$0.6	0.1

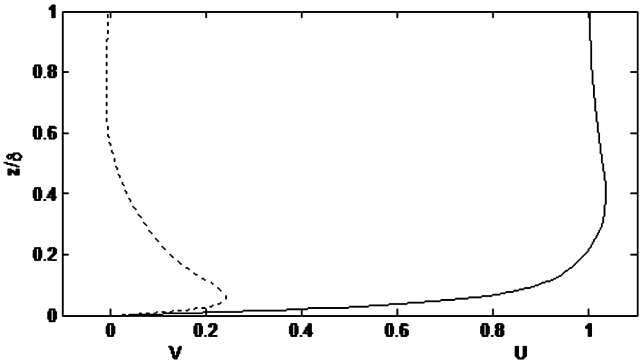

Fig. 1 Temporally and spatially averaged velocity profiles.

The flowfield was initialized using a modified laminar Ekman-layer velocity profile in which the spanwise component of the base flow was artificially reduced in magnitude, based on typical turbulent Ekman-layer velocity profiles. Fourier transformed random velocity fluctuations were added to the initial flowfield using a random distribution about an amplitude profile that decayed exponentially with the total horizontal wave number [$\alpha_{\text{total}} = (\alpha_x^2 + \alpha_y^2)$], in a manner reminiscent of a typical turbulence energy spectrum. In both cases, the maximum amplitude of the random fluctuations was on the order of 1%. The simulations were run until the flow reached a statistically steady state, based upon the total kinetic energy in the computational domain and upon the spatially averaged magnitude and direction of the surface shear stress [3]. Mean velocity profiles are provided in Fig. 1.

Turbulence statistics were collected over a sampling window of $tf \approx 6$ for both cases. The total number of time instances used for averaging was 240 for cases A and 201 for case B.

C. Validation of Direct Numerical Simulation

Verification of the results from the DNS code has been confirmed for both channel flows as well as boundary-layer problems by Marlatt and Biringen [7]. Their study allowed time-dependent inflow velocity perturbations to grow in a spanwise periodic domain that they compared with the linear theory for the stability of the laminar Ekman layer. Their results showed excellent agreement for Reynolds numbers of 65 and 100 in terms of the phase and amplitude accuracy of the numerical solution method.

III. Discussion of Results

A. Turbulence Energy Spectra

Two-dimensional Fourier spectra for each of the velocity components and the total kinetic energy (F_{uu}, F_{vv}, F_{ww}, and F_e, respectively) were computed on each horizontal plane. Contour plots of the maxima velocity and energy spectra are presented in Figs. 2 and 3 for cases A and B, respectively. The wave numbers plotted are in terms of the fundamental modes of the computational domain; wave numbers defined in terms of the characteristic length scale δ_E are related to the fundamental wave numbers by

$$\alpha_{(\delta_E)} = \frac{2\pi}{L_x}\alpha \text{ (fundamental)} \qquad (2)$$

The angle of the ridge in the contour plots may be interpreted as a measure of the preferred orientation of the most energetic flow structures for each spanwise wave number α_y. The dotted line in the figures trace the location of the peak Fourier coefficient for each α_y. Since the line is relatively straight, all of the most energetic structures appear to be characterized by the same preferred orientation. The orientation angles computed for these contours are approximately equal for both cases. These are

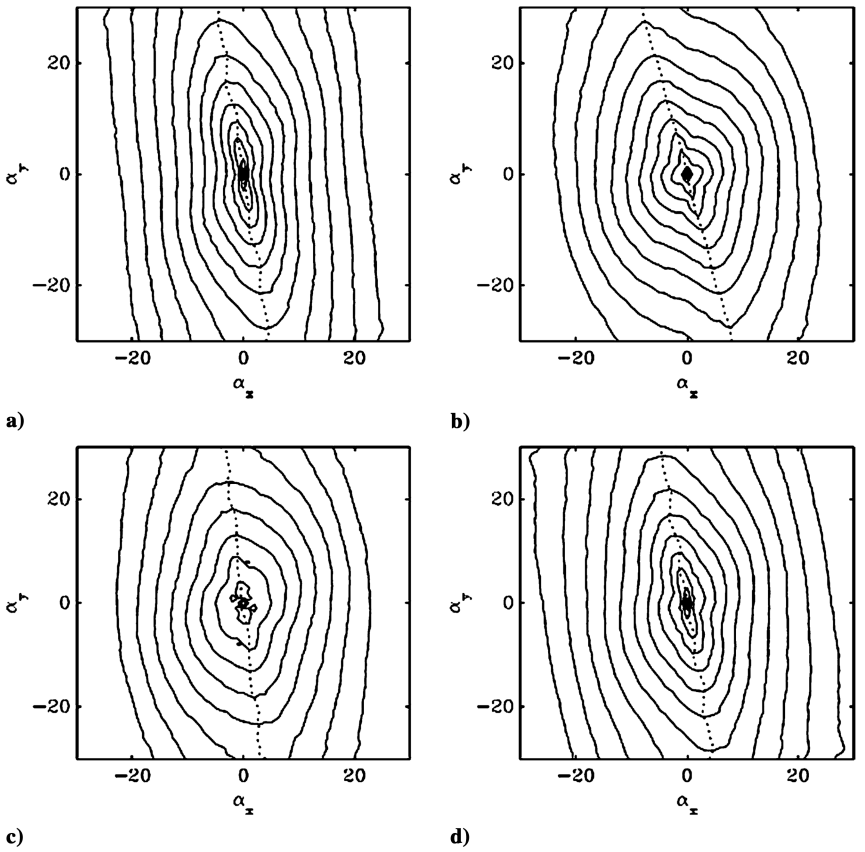

Fig. 2 Turbulent kinetic energy spectra for case A. Contours of maxima over all z for a) $\log_{10} F\overline{u'u'}$, b) $\log_{10} F\overline{v'v'}$, c) $\log_{10} F\overline{w'w'}$, and d) $\log_{10} F\bar{e}$; contour level $\Delta = 0.5$ and contour minimum is -8.0 for all plots; dotted line denotes the ridge line defined by maxima over all α_x for each α_y.

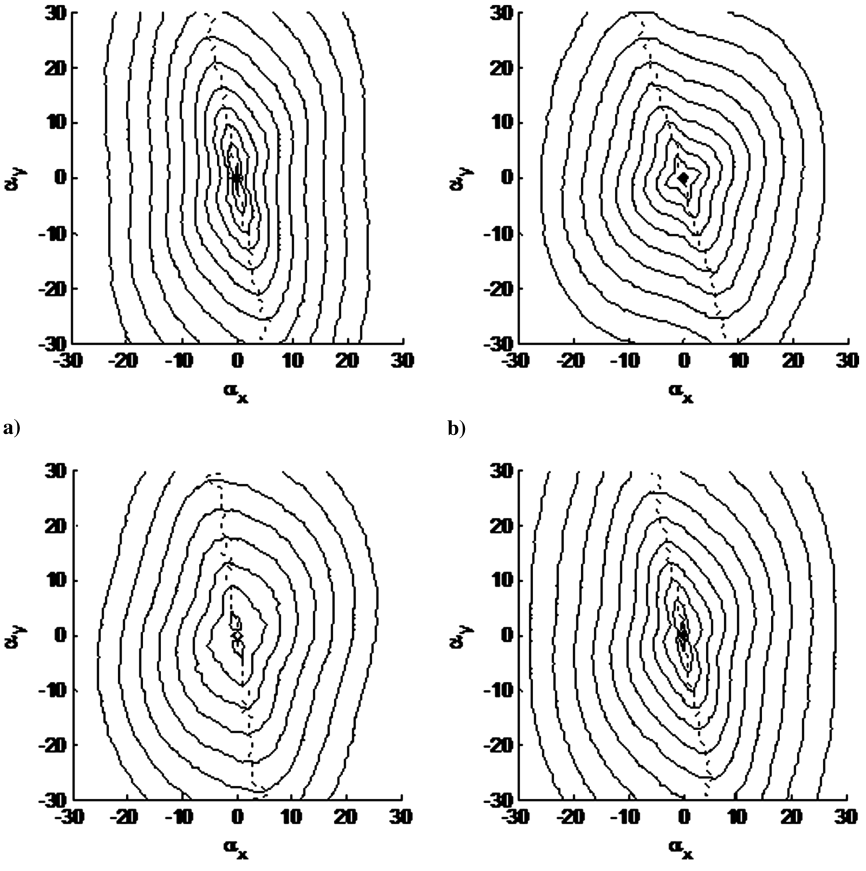

Fig. 3 Turbulent kinetic energy spectra for case B. Contours of maxima over all z for a) $\log_{10} F\overline{u'u'}$, b) $\log_{10} F\overline{v'v'}$, c) $\log_{10} F\overline{w'w'}$, and d) $\log_{10} F\bar{e}$; contour level $\Delta = 0.5$ and contour minimum is -8.0 for all plots.

$$\gamma_{uu} \approx 11^\circ, \qquad \gamma_{vv} \approx 16^\circ, \qquad \gamma_{ww} \approx 9^\circ, \qquad \gamma_e \approx 13^\circ$$

all with respect to the geostrophic flow direction. These angles are all less than the surface shear stress direction ($\beta = 28.6^\circ$) and are representative of the mean flow direction in the lower portion of the turbulent layer (from about $0.1 \leq z/\delta < 0.2$). This region corresponds to the location of strongest turbulence fluctuations indicative of distortion of turbulent structures in this region by the mean velocity.

It is notable that the orientation angle remains linear and finite throughout the entire range of spanwise wave numbers. If the small-scale structures were truly isotropic, as is generally assumed for the dissipative scales in fully turbulent flow, this angle should be close to zero at high wave numbers. Only slight straightening of the ridges can be seen in Figs. 4a, 4c, and 4d for high α_y of case B. Because the results for cases A and B are very close, indicating sufficient resolution, we attribute this deviation to a low Reynolds number effect. Typical lateral mesh spacings for Ekman-layer DNS range between values of $6 < \Delta y^+ < 10$ [5,6,8]. While the resolution of case A is slightly larger than typical grid sizes (see Table 1), the resolution of case B offers a more stringent adherence to resolution than that of comparable Ekman-layer studies.

Furthermore, the high wave numbers of case B tend to display more local isotropy when compared to case A. This is evident in the circularization of the contours given by Fig. 4. This result is in agreement with Kim and Antonia [9], whose DNS data of channel flow indicate that even at low Reynolds numbers the small scales of turbulent flow should display local isotropy.

In light of the recent reevaluation by Spalart et al. [10,11] of their $Re = 2828$ Ekman-layer DNS data, it is apparent that care must be taken to ensure grid independence of DNS solutions for the Ekman flow. Consequently, the excellent comparison observed in Figs. 2 and 3 between our high- and low-resolution simulations at $Re = 400$ give very strong evidence that the results presented here are grid-independent.

B. Turbulent Flow Budgets

Profiles of the nondimensional terms of the budget equations for the velocity variances, covariances, and turbulent kinetic energy are presented in this section. The use of direct simulation results to examine the turbulent budget equations has numerous advantages relative to an evaluation of the budget terms based on atmospheric observations. In particular, modeling of the pressure-gradient/velocity correlation term based on atmospheric data has proven extremely difficult. This term cannot be measured directly, and so it is generally derived from the budget equation balance. The error contained in the measurements of the other terms of the turbulent budget may often be in excess of the budget deficit, however, and so the confidence with which the pressure-gradient/velocity correlation may be calculated is often quite low [1]. Although improvements in measurement technology have reduced this ambiguity to some degree [12], the ability to compute all terms of the variance, covariance, and turbulent kinetic energy budgets from DNS data is of great advantage.

The general form for the energy budget equation for the velocity variances (Reynolds normal stresses) and covariances (Reynolds shear stresses) is given by Eq. (3). In the following expression, u_i are the velocity components in the x_i directions. Note that x (x_1) and y (x_2) are the horizontal coordinates and z (x_3) is the vertical coordinate.

The budget equation represents a balance between local accumulation of turbulent energy, transport by advection and by turbulent diffusion, redistribution between velocity components, and production or destruction by mean gradients:

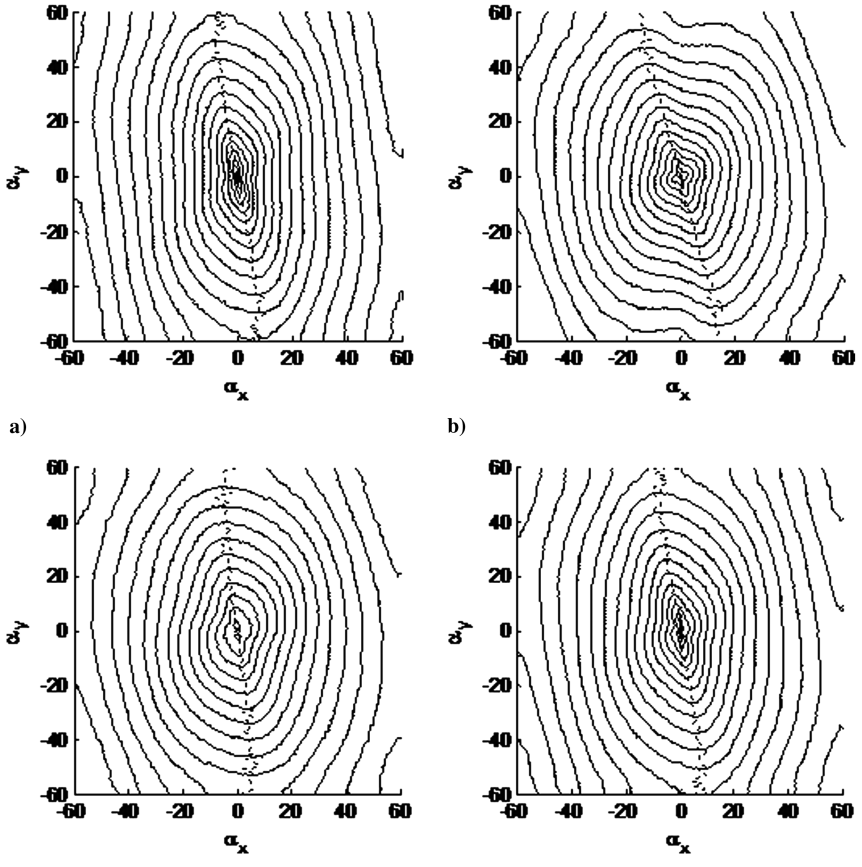

Fig. 4 Turbulent kinetic energy spectra for case B. Contours of maxima over all z for a) $\log_{10} F\overline{u'u'}$, b) $\log_{10} F\overline{v'v'}$, c) $\log_{10} F\overline{w'w'}$, and d) $\log_{10} F\bar{e}$; contour level $\Delta = 0.5$, and contour minimum is -11.0 for all plots.

$$\underbrace{\frac{\partial \overline{u_i' u_k'}}{\partial t}}_{0} = 0 = \underbrace{-\bar{u}_j \frac{\partial u_i' u_k'}{\partial x_j}}_{\mathrm{I}} + \underbrace{\overline{u_k' b'}\delta_{i3} + \overline{u_i' b'}\delta_{k3}}_{\mathrm{II}} \underbrace{-\overline{u_i' u_j'}\frac{\partial \bar{u}_k}{\partial x_j} - \overline{u_k' u_j'}\frac{\partial \bar{u}_i}{\partial x_j}}_{\mathrm{III}} \underbrace{-\frac{\partial \overline{u_i' u_j' u_k'}}{\partial x_j}}_{\mathrm{IV}} \underbrace{-\frac{2}{Re}\overline{\frac{\partial u_i'}{\partial x_j}\frac{\partial u_k'}{\partial x_j}}}_{\mathrm{V}} \underbrace{+\frac{1}{Re}\frac{\partial^2 \overline{u_i' u_k'}}{\partial x_j^2}}_{\mathrm{VI}}$$

$$\underbrace{+\overline{p'\left(\frac{\partial u_i'}{\partial x_k} + \frac{\partial u_k'}{\partial x_i}\right)}}_{\mathrm{VII}} \underbrace{-\frac{\partial \overline{u_k' p'}}{\partial x_i} - \frac{\partial \overline{u_i' p'}}{\partial x_k}}_{\mathrm{VIII}} \underbrace{+\frac{1}{Ro}(\varepsilon_{kj3}\overline{u_i' u_j'} + \varepsilon_{ij3}\overline{u_j' u_k'})}_{\mathrm{IX}} \tag{3}$$

where 0 is temporal variation; I is advection by mean shear, $A_{i,k}$; II is buoyant production/destruction of turbulent energy, $\beta_{i,k}$; III is production/destruction by mean shear stresses, $P_{i,k}$; IV is turbulent diffusion $T_{i,k}$; V is viscous dissipation $\varepsilon_{i,k}$; VI is molecular diffusion $D_{i,k}$; VII is pressure strain (return-to-isotropy) $\Phi_{i,k}$; VIII is pressure diffusion $\Theta_{i,k}$; and IX is Coriolis redistribution $C_{i,k}$.

When the ensemble averaging operator ($\bar{\ }$) is defined by averages over horizontal planes and over time, as is appropriate for the temporal simulation, and when statistically steady flow is assumed, terms 0 and I are identically zero. For the present simulation, the neutral temperature profile also implies no buoyancy forcing, and thus term II is also zero. Production of turbulent energy in the neutral Ekman layer is limited to the mean shear production term, while redistribution of turbulent energy between velocity variance components may occur through the pressure strain and the Coriolis terms. Both of these terms, when summed over all three velocity components, are identically zero for incompressible flow and are therefore absent from the turbulent kinetic energy equation. The Coriolis term is usually very small and is often omitted from the variance and covariance budgets as well, but will be included here for completeness. In addition to the above quantities, two other terms of interest are defined. The pressure strain and pressure diffusion terms may be added to produce the pressure-gradient/velocity correlation term $\Pi_{i,k}$, and the influence of molecular effects may be combined in a single term $M_{i,k}$:

$$\Pi_{i,k} = \Phi_{i,k} + \Theta_{i,k} \tag{4}$$

$$M_{i,k} = \varepsilon_{i,k} + D_{i,k} \tag{5}$$

In the profiles of the budget terms presented in the following discussion, all terms have been normalized by u_*^3/δ, where u_* is the surface friction velocity defined as $u_w = (\tau_w/\rho)^{1/2}$, τ_w is the shear stress at the wall, ρ is the density of the fluid, and $\delta = u_*/f$ (the neutral turbulent depth).

C. Variance Budgets

Prognostic equations for the velocity variances (normal Reynolds stresses) may be computed by multiplying each momentum equation by its associated velocity component, expressing the flowfield variables as the sum of a mean plus perturbation, and Reynolds averaging the resulting equation. Profiles of the terms of the variance budgets are presented in Figs. 5–8 for $\overline{u'u'}$, $\overline{v'v'}$, and $\overline{w'w'}$. In each figure, details of the wall region ($z \le 0.2\delta$, $z^+ < 70$) and the far-field region of the boundary layer ($0.2\delta < z < \delta$) are shown (note that z^+ is defined as $z^+ = zu_*/\nu$).

1. *Streamwise Variance Energy Budget* $\overline{u'u'}$

Vertical profiles of the terms of the energy budget for the streamwise velocity variance $\overline{u'u'}$ are presented in Figs. 5 and 6 for cases A and B, respectively. In each figure, subplot *a* represents the near-wall region, and *b* illustrates the far-field behavior. Consistency between cases A and B is clearly evident as the budgets are nearly identical apart from small amplitude differences. It is believed that these are simply due to finite sampling of random fluctuations in turbulent fields. Similar consistency between cases A and B was noted for all other variance and covariance budgets. For brevity, the case A budgets have been omitted for the remaining terms.

The vertical structure of the $\overline{u'u'}$ budget is characterized by a peak in turbulent production by mean shear at $z^+ \approx 12$, close to the location of the maximum mean spanwise velocity. At this point, the production is balanced primarily by viscous dissipation and turbulent diffusion, in similar proportion. Extrema in the pressure strain and Coriolis terms are associated with this maximum, while the minimum molecular diffusion occurs slightly closer to the wall. The local extrema in both the molecular and turbulent diffusion terms indicate rapid transport of turbulent energy away from the location of maximum production, while the extrema in the pressure strain and Coriolis terms indicate redistribution of turbulent energy to $\overline{v'v'}$ and $\overline{w'w'}$ (the destination of this energy will be described in the following sections). The pressure diffusion term is identically zero for this component of the normal Reynolds stress. At the wall, dissipation is balanced by molecular diffusion. Although turbulent diffusion is zero at the wall, this term becomes positive immediately above the wall, indicating turbulent transport of streamwise turbulent energy toward the wall. In the far field, the $\overline{u'u'}$ production term decays more readily than does dissipation, leaving the energy balance dominated by dissipation and turbulent diffusion. The pressure strain profile for the budget is negative for the majority of the domain, indicating that turbulent energy is distributed from $\overline{u'u'}$ to the other normal stress components.

The profiles described here agree qualitatively with those presented by Spalart [13] for the Ekman-like boundary-layer DNS, including the sign change in the pressure strain term between the near-wall region and the far field [13]. The sign change in turbulent diffusion observed by Spalart for the nonrotating boundary layer does not appear in this case [14] and was similarly absent in the compressible boundary-layer simulation by Hatay and Biringen [15], who attributed the difference to the lower Reynolds number of [13]. A similar conjecture is made here.

2. *Spanwise Variance Energy Budget* $\overline{v'v'}$

Profiles for the spanwise Reynolds normal stress are shown in Figs. 7a and 7b. In contrast to the nonrotating boundary layer, the spanwise energy balance includes production of turbulence due to mean shear. In this case, a local maximum in the turbulent production near $z^+ \approx 8$ is associated with a local decrease in dissipation but an increased rate of molecular diffusion, and a maximum in the pressure strain term. A small extrema in redistribution due to Coriolis transfer is also noted, though as in the $\overline{u'u'}$ budget, the direct effect of rotation on the normal Reynolds stress budget is nearly an order of magnitude smaller than the other terms. (The indirect effects, however, are significant, as the existence of the mean spanwise velocity component and therefore $\overline{v'v'}$ production, is by no means negligible.) A second, larger, maximum in the spanwise production term occurs at $z^+ \approx 60$. This region of production is much broader vertically than is the lower region and does not particularly stand out in Fig. 7. This production region is also in very close equilibrium with the $\overline{v'v'}$ dissipation. In the far field, production is generally balanced by dissipation until $z \approx 0.8\delta$, after which point the production decays more rapidly than does turbulent diffusion (reminiscent of the streamwise normal stress budget). The pressure diffusion term for this component is again identically zero; the pressure strain is mostly positive, indicating its effect as a source of turbulent energy, transferred from the streamwise variance budget. The Coriolis term is, in contrast, negative and redistributes energy from the $\overline{v'v'}$ budget to the streamwise variance balance.

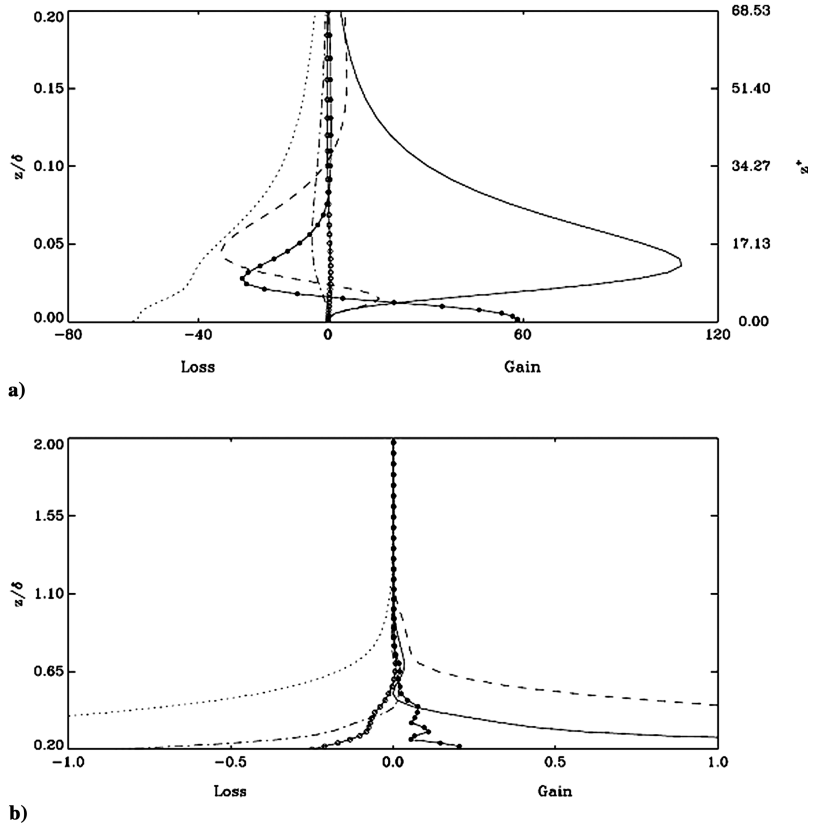

Fig. 5 Vertical profiles of the terms of the $\overline{u'u'}$ variance budget for case A profiles: a) near wall and b) far field. All terms have been nondimensionalized by u_*^3/δ; production by mean shear $P_{1,1}$ (solid line), turbulent diffusion $T_{1,1}$ (dashed line), viscous dissipation $\varepsilon_{1,1}$ (dotted line), molecular diffusion $D_{1,1}$ (black circles), pressure strain $\Phi_{1,1}$ (dotted–dashed line), and Coriolis redistribution $C_{1,1}$ (white circles).

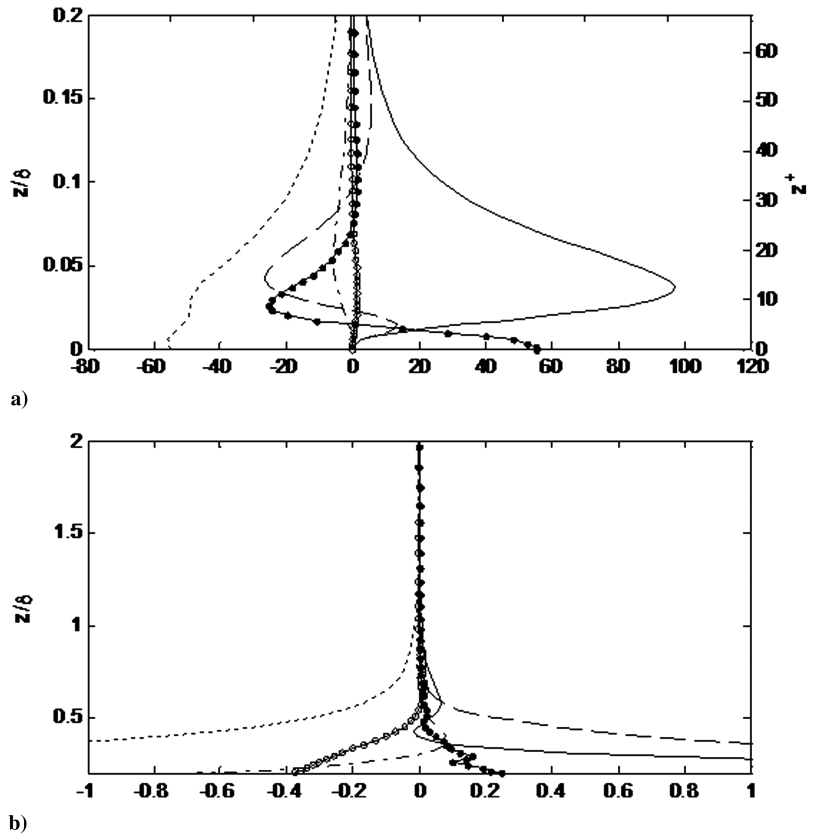

Fig. 6 Vertical profiles of the terms of the $\overline{u'u'}$ variance budget for case B profiles: a) near wall and b) far field. All terms have been nondimensionalized by u_*^3/δ; production by mean shear $P_{1,1}$ (solid line), turbulent diffusion $T_{1,1}$ (dashed line), viscous dissipation $\varepsilon_{1,1}$ (dotted line), molecular diffusion $D_{1,1}$ (black circles), pressure strain $\Phi_{1,1}$ (dotted–dashed line), and Coriolis redistribution $C_{1,1}$ (white circles).

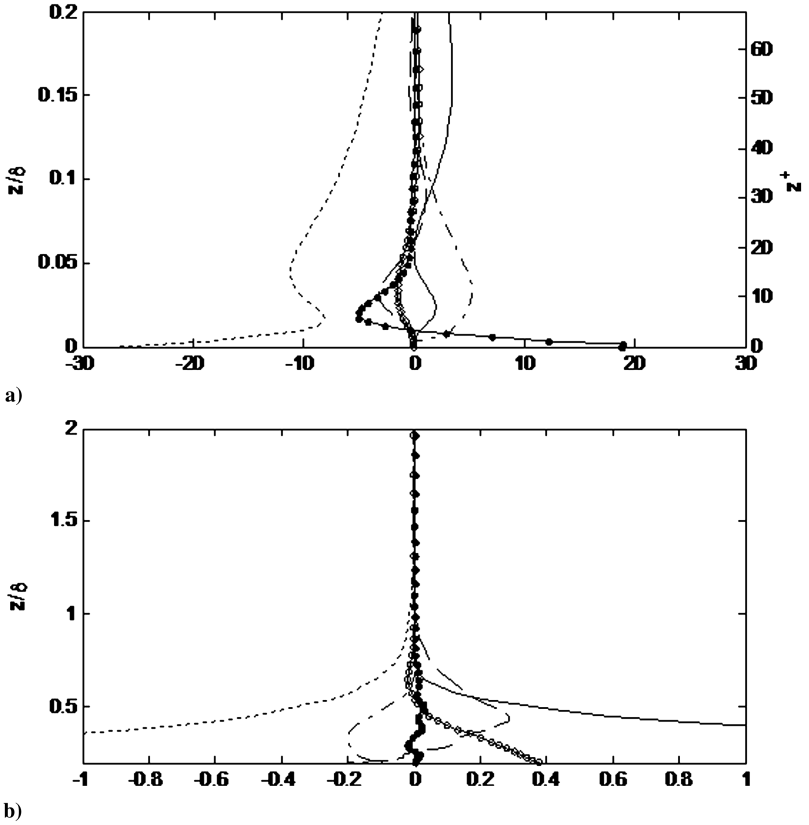

Fig. 7 Vertical profiles of the terms of the $\overline{v'v'}$ variance budget for case B profiles: a) near wall and b) far field. All terms have been nondimensionalized by u_*^3/δ; production by mean shear $P_{2,2}$ (solid line), turbulent diffusion $T_{2,2}$ (dashed line), viscous dissipation $\varepsilon_{2,2}$ (dotted line), molecular diffusion $D_{1,1}$ (black circles), pressure strain $\Phi_{2,2}$ (dotted–dashed line), and Coriolis redistribution $C_{2,2}$ (white circles).

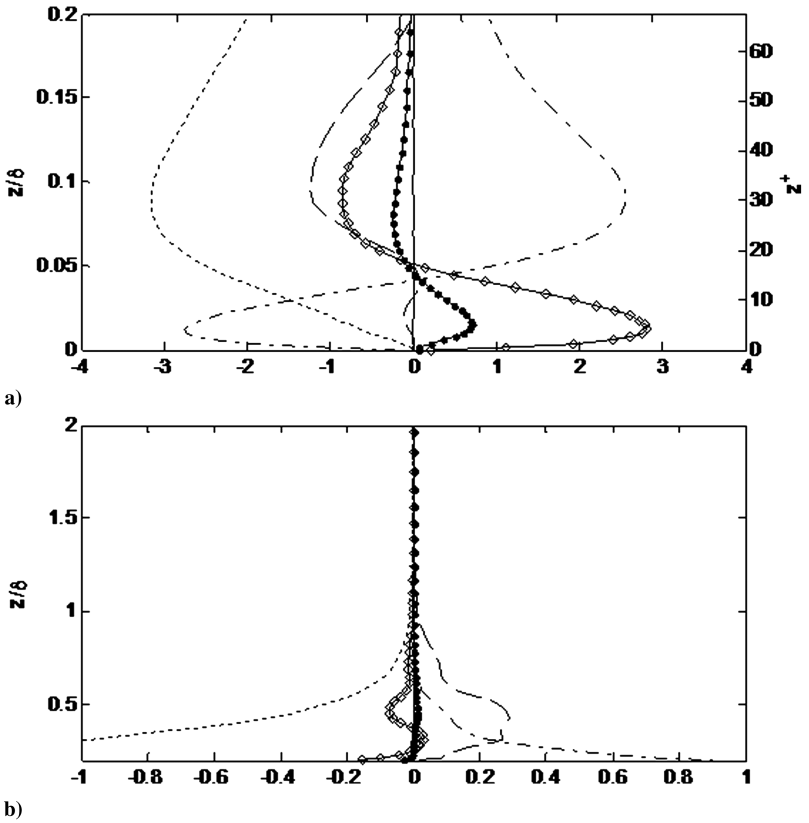

Fig. 8 Vertical profiles of the terms of the $\overline{w'w'}$ variance budget for case B profiles: a) near wall and b) far field. All terms have been nondimensionalized by u_*^3/δ; production by mean shear $P_{3,3}$ (solid line), turbulent diffusion $T_{3,3}$ (dashed line), viscous dissipation $\varepsilon_{3,3}$ (dotted line), molecular diffusion $D_{3,3}$ (black circles), pressure strain $\Phi_{3,3}$ (dotted–dashed line), and pressure diffusion $\Theta_{3,3}$ (diamonds).

3. Vertical Variance Energy Budget $\overline{w'w'}$

The terms of the vertical component of the normal Reynolds stress balance are presented in Figs. 8a and 8b. The $\overline{w'w'}$ component has no shear production, so the only source of energy is from intermodal redistribution via the pressure strain term. The pressure strain is positive, representing an energy source, throughout most of the boundary layer. Near the wall, however, the sign of the pressure strain and of the pressure diffusion terms change, and energy is transferred from the vertical variance to the horizontal components. This process is characteristic of turbulent boundary layers and was given the term splatting effect by Moin and Kim [16]. The molecular diffusion peaks near the maximum splatting region (close to $z^+ \approx 5$), as does the pressure diffusion term. Turbulent diffusion, in contrast, is effectively zero from the wall to the location of the pressure strain sign change at $z^+ \approx 15$. This also is characteristic of turbulent boundary layers [15]. In the far field (Fig. 8b), the vertical normal stress budget is primarily balanced by turbulent diffusion and dissipation.

4. Turbulent Energy Redistribution

Details of the redistribution of turbulent energy between the $\overline{u'u'}$, $\overline{v'v'}$, and $\overline{w'w'}$ components of the kinetic energy budget are shown in Fig. 9a, while the relative magnitudes of the pressure strain, pressure diffusion, and pressure-gradient/velocity correlation terms of the $\overline{w'w'}$ budget are shown in Fig. 9b. The splatting effect described in the preceding paragraph is clearly observed in Fig. 9a. As high-momentum fluid descends toward the wall, energy is redistributed primarily to the spanwise energy component, although a very small increase is noted in the streamwise component very near the wall ($z^+ < 2$, with maximum magnitude 0.168). Integrated over the height of the domain, the streamwise component distributes nearly equal energy to the spanwise and vertical components: ≈58% to $\overline{v'v'}$, and ≈42% to $\overline{w'w'}$. From an examination of the vertical profiles, it appears that this distribution is primarily from the streamwise to vertical variances away from the wall and from the vertical component to the spanwise in the splatting region. The streamwise Coriolis redistribution term is also plotted here; the spanwise profile is simply of opposite sign. Near the wall, the system rotation acts to transfer turbulent energy from the spanwise component to the streamwise, whereas away from the wall (above $z^+ \approx 27$), the opposite is true. Integrated over the height of the domain, the total transfer via the Coriolis terms is only about 4% of the pressure strain redistribution; however, the maximum value of the Coriolis term is nearly 14% of the maximum pressure strain, so at least for this flow, neglect of the rotation term from the variance budgets would be unwise.

D. Covariance Budgets

1. Primary Reynolds Stress Budgets $-\overline{u'w'}$ and $-\overline{v'w'}$

The Ekman layer is characterized by two components of the primary Reynolds stress: $-\overline{u'w'}$ and $-\overline{v'w'}$. The streamwise and spanwise shear stress components provide the source of mean shear turbulent energy production in the streamwise and spanwise variance equations, respectively, and an analysis of the budgets of each of these contributors lends additional understanding of the mechanisms that control the turbulent Ekman layer.

Vertical profiles of the streamwise primary Reynolds shear stress budget $-\overline{u'w'}$ are shown in Figs. 10a and 10b. The maximum production occurs at the same location as the streamwise normal stress production maximum, as expected from the explicit coupling between these budgets. At this point, the production is balanced primarily by turbulent diffusion, which transfers turbulent stress upwards. Pressure strain is also relatively large at this point (about half that of the turbulent diffusion), and acts to transfer energy to the other shear stress components. The pressure strain represents a loss for most of the wall region, but exhibits a sign change at $z^+ \approx 100$ and provides positive contributions through the remainder of the

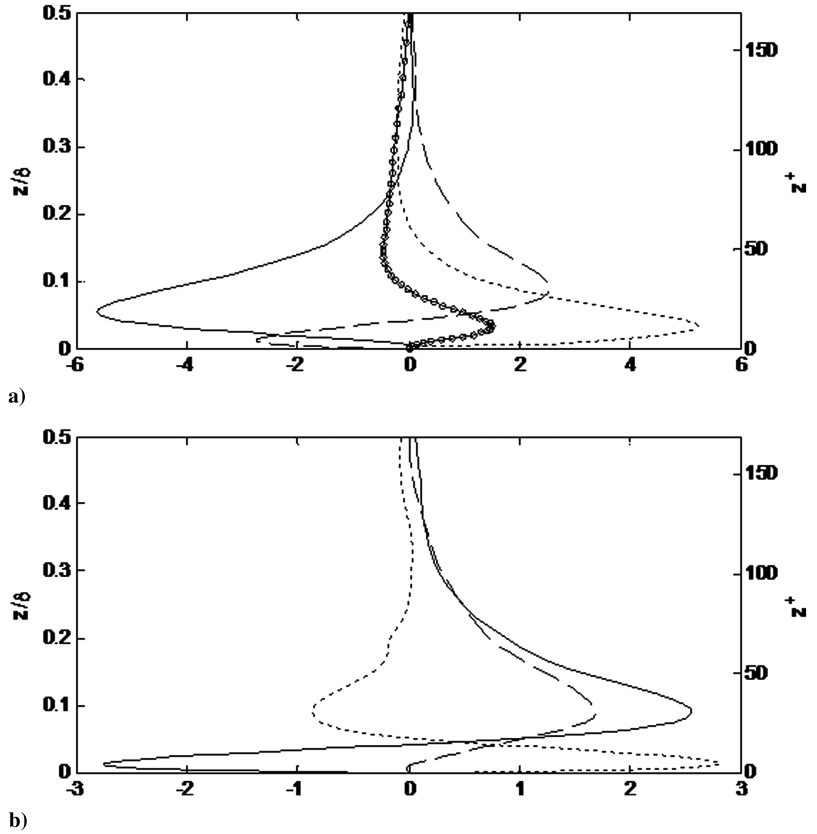

Fig. 9 Vertical profiles of the terms of the intercomponent energy redistribution terms for the case B velocity variance budgets: a) $\overline{u'u'}$ pressure strain $\Phi_{1,1}$ (solid line), $\overline{v'v'}$ pressure strain $\Phi_{2,2}$ (dotted line), $\overline{w'w'}$ pressure strain $\Phi_{3,3}$ (dashed line); and $\overline{u'u'}$ Coriolis redistribution $C_{1,1}$ (white circles), and b) pressure-gradient/velocity correlations for the $\overline{w'w'}$ budget: pressure strain $\Phi_{3,3}$ (solid line), pressure diffusion $\Theta_{3,3}$ (dotted line), and sum $\Pi_{3,3}$ (dashed line). All terms have been nondimensionalized by u_*^3/δ.

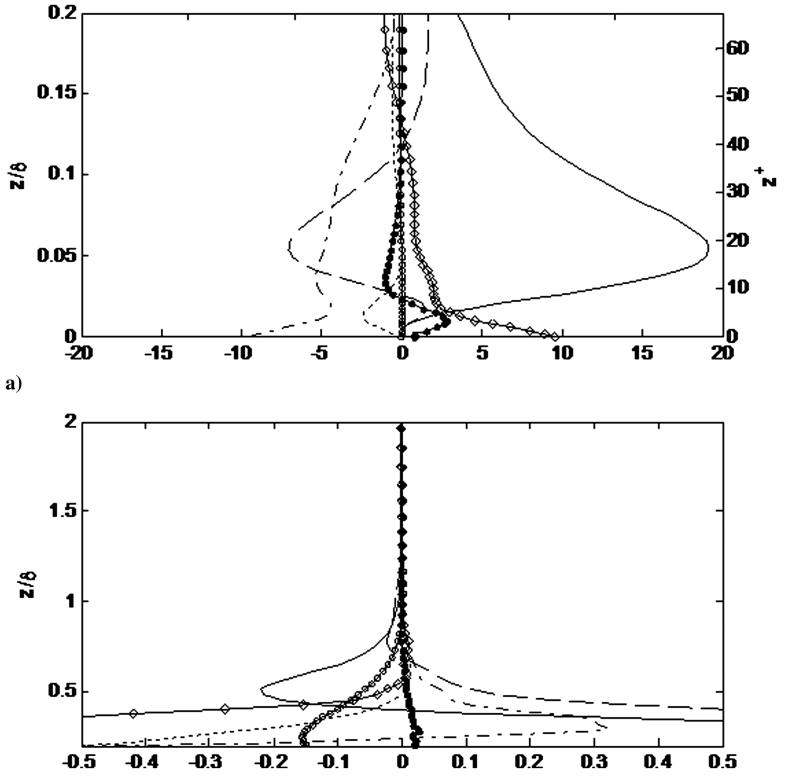

Fig. 10 Vertical profiles of the terms of the $\overline{u'w'}$ covariance budget for case B profiles: a) near wall and b) far field. All terms have been nondimensionalized by u_*^3/δ: production by mean shear $P_{1,3}$ (solid line), turbulent diffusion $T_{1,3}$ (dashed line), viscous dissipation $\varepsilon_{1,3}$ (dotted line), molecular diffusion $D_{1,3}$ (black circles), pressure strain $\Phi_{1,3}$ (dotted-dashed line), pressure diffusion $\Theta_{1,3}$ (diamonds), and Coriolis redistribution $C_{1,3}$ (white circles).

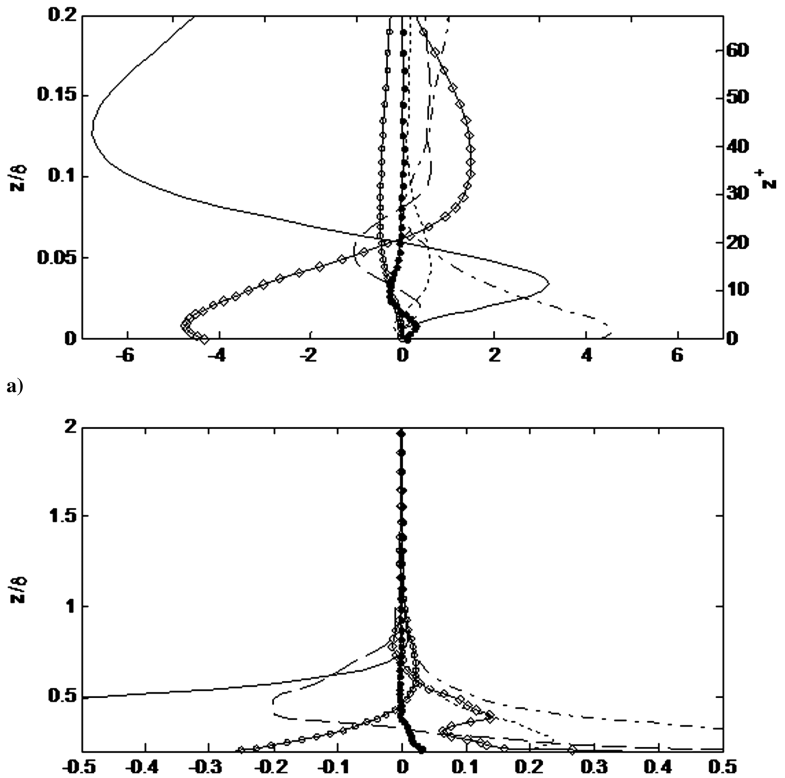

Fig. 11 Vertical profiles of the terms of the $\overline{v'w'}$ covariance budget for case B profiles: a) near wall and b) far field. All terms have been nondimensionalized by u_*^3/δ: production by mean shear $P_{2,3}$ (solid line), turbulent diffusion $T_{2,3}$ (dashed line), viscous dissipation $\varepsilon_{2,3}$ (dotted line), molecular diffusion $D_{2,3}$ black circles), pressure strain $\Phi_{2,3}$ (dotted-dashed line), pressure diffusion $\Theta_{2,3}$ (diamonds), and Coriolis redistribution $C_{2,3}$ (white circles).

turbulent layer. Dissipation is very weak throughout the layer, as are the effects of rotation. Molecular diffusion is also very weak at the wall, and remains ineffective throughout the boundary layer. At the wall, the budget represents a balance between pressure strain and pressure diffusion: turbulent energy is diffused downward primarily by the pressure velocity correlation, and redistributed to other components via the pressure strain term in the near-wall layer.

The spanwise primary Reynolds shear stress $-\overline{v'w'}$ contributes directly to the kinetic energy budget via the spanwise variance production term. Vertical profiles of the budget terms are shown in Figs. 11a and 11b; as in the $-\overline{u'w'}$ budget, the wall layer is dominated by a balance between pressure diffusion and pressure strain, but here the roles are reversed and turbulent energy is provided to the spanwise shear stress budget through the pressure strain redistribution, and transferred upward by the pressure diffusion. Shear production represents a gain near the wall but, in contrast with the streamwise shear, changes sign at $z^+ \approx 20$, where the sign of the vertical derivative of the mean spanwise velocity becomes negative. Molecular diffusion and Coriolis transfer terms remain small over the majority of the boundary layer, as does viscous dissipation. Away from the wall ($z^+ > 20$), the budget is dominated by loss due to the shear production term and is balanced in roughly equal measure by turbulent diffusion, pressure diffusion, and pressure strain and, to a smaller degree, by viscous effects. The Coriolis term represents a small loss when integrated over the entire boundary layer, though a sign change in this term in the upper portion of the turbulent layer corresponds to a similar event in the $-\overline{u'v'}$ budget and indicates a positive energy transfer from the secondary Reynolds shear stress budget.

2. *Secondary Reynolds Stress Budget* $-\overline{u'v'}$

The secondary Reynolds stress $\overline{u'v'}$ represents an important contribution to the dynamics of secondary flow [17]. While the budget of the secondary Reynolds shear stress may not be as important to the present simulation as the primary shear stress budgets, it is expected to be of considerable interest in the analysis of turbulent Ekman layers over inhomogeneous surfaces, and, therefore, evaluation of the secondary shear stress terms provides a basis of comparison for such flowfields. Although the secondary shear stress term appears explicitly in the Coriolis terms of the normal stress equations, it does not contribute to turbulence production and only provides an avenue for energy redistribution. However, when horizontal homogeneity is not assumed, $-\overline{u'v'}$ production terms appear in the $\overline{u'u'}$ and $\overline{v'v'}$ variance balances, and the secondary shear stress may contribute to the total turbulent kinetic energy budget.

Vertical profiles of the secondary shear stress balance terms are shown in Figs. 12a and 12b for the near-wall and far-field regions, respectively. It is interesting to note that although the secondary stress does not contribute to the total kinetic energy budget, the maximum (absolute) production ($\approx$15 at $z^+ \approx 10$) is of the same order of magnitude as observed in the primary shear stress profiles ($\approx$19 at $z^+ \approx 18$ for $-\overline{u'w'}$ and $\approx$7 at $z^+ \approx 40$ for $-\overline{v'w'}$). The production term for $-\overline{u'v'}$ represents a loss in the near-wall region, and a gain for $z^+ > 20$. At the wall, dissipation balances molecular diffusion, while the turbulent diffusion and Coriolis terms become large near the location of the production minimum. Note that while in the lateral variance budgets the Coriolis term was generally much less than all other contributions to the normal stress budget equations, the influence of rotation is close to the same order as the other terms here. Farther away from the surface, production gains are generally balanced by a combination of turbulent diffusion and pressure strain throughout the rest of the turbulent layer (the pressure diffusion term is identically zero for the laterally homogeneous form of this budget). At the very top of the turbulent layer, a small reversal in the production term is noted, where the contribution of mean shear again constitutes a loss to the $-\overline{u'v'}$ balance. The sign reversal in the Coriolis term at $z \approx 0.45\delta$ corresponds to a similar event in the $-\overline{v'w'}$ budget and indicates a loss of energy from $-\overline{u'v'}$ to the spanwise primary stress budget.

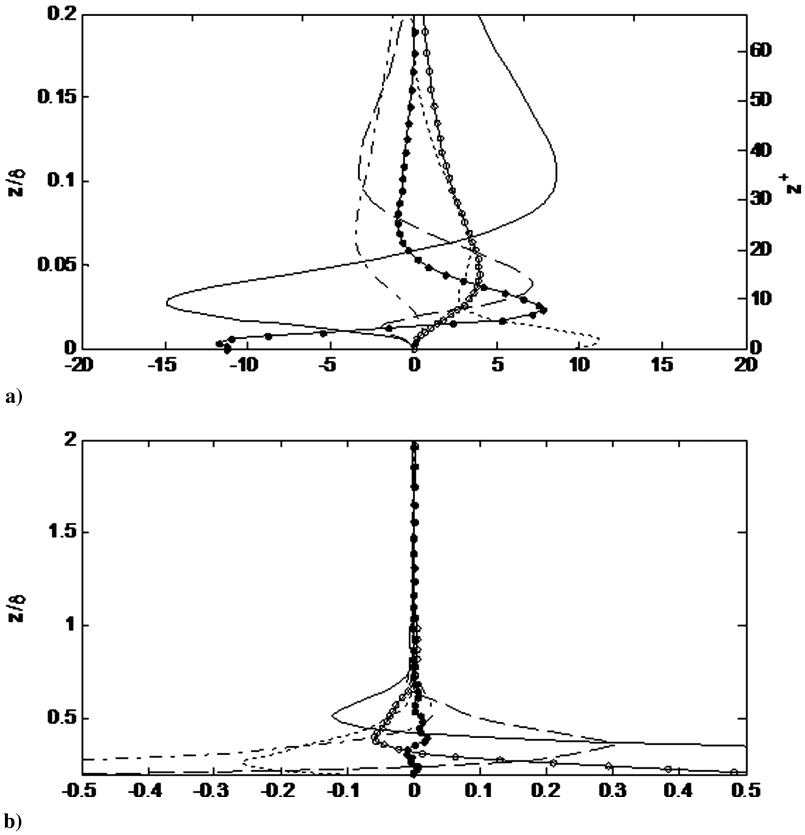

Fig. 12 Vertical profiles of the terms of the $\overline{u'v'}$ covariance budget for case B profiles: a) near wall and b) far field. All terms have been nondimensionalized by u_*^3/δ: production by mean shear $P_{1,2}$ (solid line), turbulent diffusion $T_{1,2}$ (dashed line), viscous dissipation $\varepsilon_{1,2}$ (dotted line), molecular diffusion $D_{1,2}$ (black circles), pressure strain $\Phi_{1,2}$ (dotted–dashed line), and Coriolis redistribution $C_{1,2}$ (white circles).

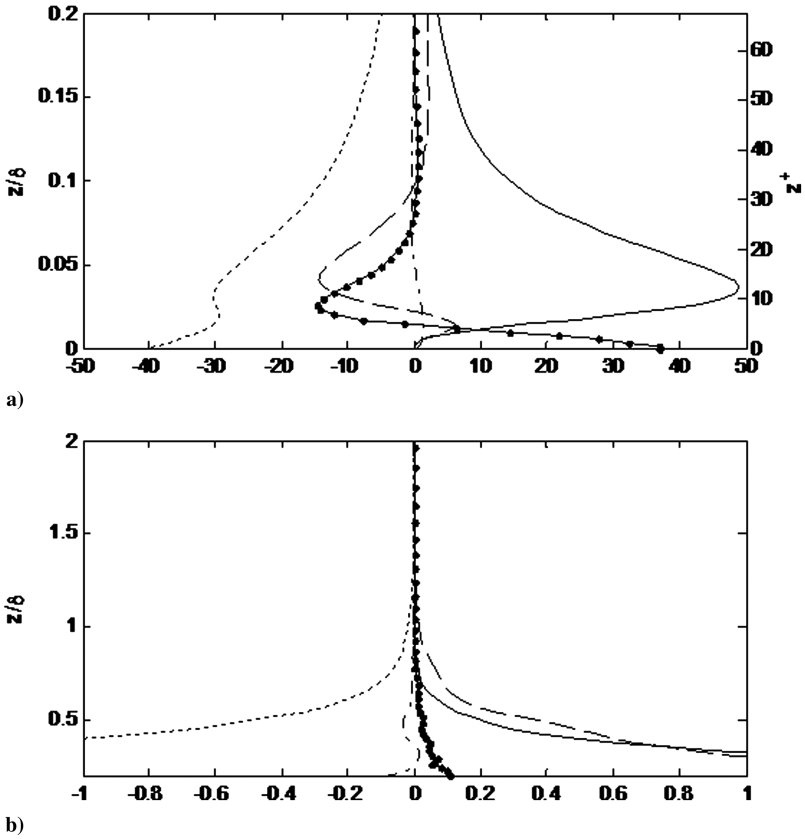

Fig. 13 Vertical profiles of the terms of the turbulent kinetic energy budget for case B profiles: a) near wall and b) far field. All terms have been nondimensionalized by u_*^3/δ: production by mean shear $P_{0,0}$ (solid line), turbulent diffusion $T_{0,0}$ (dashed line), viscous dissipation $\varepsilon_{0,0}$ (dotted line), molecular diffusion $D_{0,0}$ (black circles), and pressure diffusion $\Theta_{0,0}$ (dotted–dashed lines).

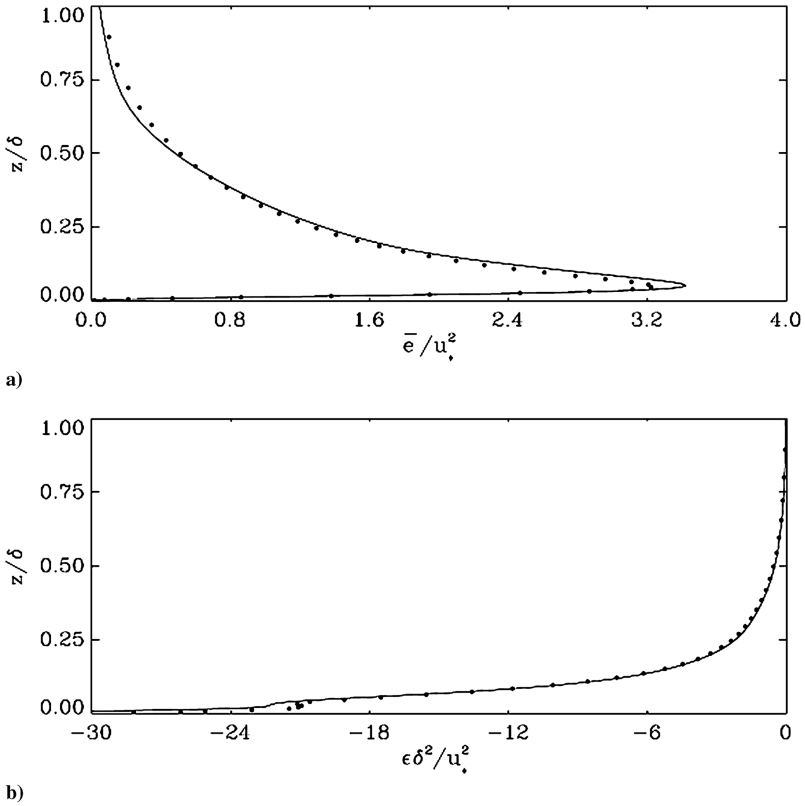

Fig. 14 Case A profiles of a) turbulent kinetic energy $\bar{e}$ and b) viscous dissipation ε; present results (solid line) and Coleman et al. [2] (black circles).

E. Turbulent Kinetic Energy Budget

The turbulent kinetic energy budget (given by $\bar{e} = \frac{1}{2}\overline{u_i' u_i'}$, where the repeated indices denote a summation), shown for the near wall and far field in Figs. 13a and 13b, exhibits near equilibrium balance, with an integrated discrepancy of less than 1%. Turbulent energy production is a maximum near $z^+ \approx 15$ and is effectively represented by the streamwise variance production. At this point the production is balanced primarily by dissipation, although loss contributions from molecular and turbulent diffusion together have a greater effect than does the dissipation. As was noted in the variance budgets, the dissipation is balanced by molecular diffusion near the wall, the latter term transporting turbulent energy from the region directly above the wall down to the wall layer. Turbulent diffusion also contributes to the downward transfer of turbulence below $z^+ \approx 8$; farther away from the wall, but below $z^+ \approx 35$, both turbulent and molecular diffusion act to transport turbulence upward across the boundary layer. Above this point, molecular diffusion is very weak, and the turbulent transfer term again changes sign and downward energy diffusion is observed. In the far field, the production decays more rapidly than does the dissipation, as noted for the variance budgets, and above the turbulent layer an approximate balance is obtained between dissipation and turbulent transfer. Note that the turbulent energy redistribution terms, pressure strain and Coriolis effects, are absent in the $\bar{e}$ budget; these terms act to exchange energy between the normal stress components, but do not contribute to the total kinetic energy in the flow. (The turbulent kinetic energy and dissipation show excellent agreement with the results from Coleman et al. [2], as demonstrated by Fig. 14.)

IV. Conclusions

The results of a numerical simulation of the neutrally stratified, turbulent Ekman layer have been examined in considerable detail. These results illuminate a number of interesting aspects of the dynamics of this flow.

The simulation results presented here agree very well with those of Coleman et al. [2,18]. This provides considerable credibility to both their work and to the present results, as the numerical solution methods used to integrate the flowfields were quite different. The differences noted in the surface shear direction and friction velocity serve to confirm their estimates of the accuracy with which these are computed by direct simulation (about 3 and 1%, respectively).

The direction of the Reynolds stress vector is shown to be oriented at a generally oblique angle to the mean velocity shear stress direction. In the lower third of the boundary layer, where turbulence is strongest, the angle between these quantities is often as large as 50° and suggests that turbulence models that assume parallel stress vectors may provide inaccurate estimates of the turbulence shear stress.

A significant new finding of this work indicates that, according to the $\overline{u'v'}$ budget analysis, secondary Reynolds stresses cannot be neglected concerning energy transport. This term provides an avenue for energy redistribution that is close to the same magnitude as $-\overline{u'w'}$ or $-\overline{v'w'}$.

The direct simulation results allowed a detailed presentation of the turbulent kinetic energy budget profiles, including budget analyses for the contributing variances and covariances. It is demonstrated that the majority of turbulent kinetic energy in this flow is produced by coupling between the streamwise primary Reynolds shear stress $\overline{u'w'}$ and the streamwise velocity gradient. This energy is transferred in the boundary-layer interior to vertical velocity fluctuations through the pressure-gradient/velocity correlation terms. Near the wall, coupling of the vertical velocity variances with the spanwise allows a transfer of kinetic energy by means of the return-to-isotropy pressure strain terms, in what has been described as the splatting effect.

Acknowledgments

The majority of this work was completed at the University of Colorado at Boulder under an Advanced Studies Program sponsored by the University Corporation for Atmospheric Research. Computer resources were provided by both the National Center for Atmospheric Research and the San Diego Supercomputing Center. The authors would like to thankfully acknowledge the support of James C. McWilliams (National Center for Atmospheric Research, Boulder).

References

[1] Stull, R. B., *An Introduction to Boundary Layer Meteorology*, Kluwer Academic, Dordrecht, The Netherlands, 1988.

[2] Coleman, G. N., Ferziger, J. H., and Spalart, "A Numerical Study of the Ekman Layer," *Journal of Fluid Mechanics*, Vol. 213, 1990, pp. 313–348.
doi:10.1017/S0022112090002348

[3] Marlatt, S. W., "Direct Numerical Simulation of Ekman Layer Transition and Turbulence," Ph.D. Thesis, Univ. of Colorado, Boulder, CO, 1994.

[4] Tennekes, H., and Lumley, J. L., *A First Course in Turbulence*, M.I.T. Press, Cambridge, MA, 1972.

[5] Coleman, G. N., "Similarity Statistics from a Direct Numerical Simulation of the Neutrally Stratified Planetary Boundary Layer," *Journal of the Atmospheric Sciences*, Vol. 56, Mar. 1999, pp. 891–900.
doi:10.1175/1520-0469(1999)056<0891:SSFADN>2.0.CO;2

[6] Taylor, J. R., and Sarkar, S., "Direct and Large Eddy Simulations of a Bottom Ekman Layer Under an External Stratification," *International Journal of Heat and Fluid Flow*, Vol. 29, 2008, pp. 721–732.
doi:10.1016/j.ijheatfluidflow.2008.01.017

[7] Marlatt, S. W., and Biringen, S., "Spatial Simulation of Secondary Instability in the Laminar Ekman Layer," 32nd Aerospace Sciences Meeting & Exhibit, Reno, NV, AIAA Paper 1994-0828, 1994.

[8] Miyahita, K., Iwamoto, K., and Kawamura, H., "Direct Numerical Simulation of the Neutrally Stratified Turbulent Ekman Boundary Layer," *Journal of the Earth Simulator*, Vol. 6, Oct. 2006, pp. 3–15.

[9] Kim, J., and Antonia, R. A., "Isotropy of the Small Scales of Turbulence at Low Reynolds Numbers," *Journal of Fluid Mechanics*, Vol. 251, 1993, pp. 219–238.
doi:10.1017/S0022112093003398

[10] Spalart, P. R., Coleman, G. N., and Johnstone, R., "Retraction: Direct Numerical Simulation of the Ekman Layer: A Step in Reynolds Number, and Cautious Support for a Log Law with a Shifted Origin," *Physics of Fluids*, Vol. 21, 2009, Paper 109901.
doi:10.1063/1.3247176

[11] Spalart, P. R., Coleman, G. N., and Johnstone, R., "Direct Numerical Simulation of the Ekman Layer: A Step in Reynolds Number, and Cautious Support for a Log Law with a Shifted Origin," *Physics of Fluids*, Vol. 20, No. 10, 2008, Paper 101507.
doi:10.1063/1.3005858

[12] Wilczak, J. M., Oncley, S. P., and Bedard, A. J., Jr., "Turbulent Pressure Fluctuations in the Atmospheric Surface Layer," *Proceedings of the Tenth Symposium on Turbulence and Diffusion*, American Meteorological Society, Boston, 1992, pp. 167–170.

[13] Spalart, P. R., "Theoretical and Numerical Study of a Three-Dimensional Turbulent Boundary Layer," *Journal of Fluid Mechanics*, Vol. 205, 1989, pp. 319–340.
doi:10.1017/S0022112089002053

[14] Spalart, P. R., "Direct Numerical Simulation of a Turbulent Boundary Layer up to $Re_\theta = 1410$," *Journal of Fluid Mechanics*, Vol. 187, 1988, pp. 61–98.
doi:10.1017/S0022112088000345

[15] Hatay, F., and Biringen, S., "Direct Numerical Simulation of Low Reynolds Number Supersonic Shear Layers II: Statistical Analysis and Energy Budgets," *International Journal of Fluid Mechanics Research*, Vol. 26, No. 1, 1999, pp. 17–35.

[16] Moin, P., and Kim, J., "Numerical Investigation of Turbulent Channel Flow," *Journal of Fluid Mechanics*, Vol. 118, 1982, pp. 341–377.
doi:10.1017/S0022112082001116

[17] Huser, A., and Biringen, S., "Direct Numerical Simulation of Turbulent Flow in a Square Duct," *Journal of Fluid Mechanics*, Vol. 257, 1993, pp. 339–358.
doi:10.1017/S0022112093003106

[18] Coleman, G. N., Ferziger, J. H., and Spalart, P. R., "A Numerical Study of the Ekman Layer," *Journal of Fluid Mechanics*, Vol. 213, 1990, pp. 313–348.
doi:10.1017/S0022112090002348